

Horizontal flow fields observed in *Hinode* G-band images

II. Flow fields in the final stages of sunspot decay

M. Verma¹, H. Balthasar¹, N. Deng^{2,3}, C. Liu², T. Shimizu⁴, H. Wang², and C. Denker¹

¹ Leibniz-Institut für Astrophysik Potsdam (AIP), An der Sternwarte 16, 14482 Potsdam, Germany
e-mail: mverma@aip.de, hbalthasar@aip.de, cdenker@aip.de

² New Jersey Institute of Technology, Space Weather Research Laboratory, 323 Martin Luther King Blvd., Newark, NJ 07102, USA
e-mail: nd7@njit.edu, chang.liu@njit.edu, haimin.wang@njit.edu

³ California State University Northridge, Physics and Astronomy Department, 18111 Nordhoff St., Northridge, CA 91330, USA

⁴ Institute of Space and Astronautical Science, Japan Aerospace Exploration Agency, 3-1-1 Yoshinodai, Chuo-ku, Sagami-hara, Kanagawa 252-5210, Japan
e-mail: shimizu.toshifumi@isas.jaxa.jp

Received August 08, 2011; accepted December 02, 2011

ABSTRACT

Context. Generation and dissipation of magnetic fields is a fundamental physical process on the Sun. In comparison to flux emergence and the initial stages of sunspot formation, the demise of sunspots still lacks a comprehensive description.

Aims. The evolution of sunspots is most commonly discussed in terms of their intensity and magnetic field. Here, we present additional information regarding the three-dimensional flow field in the vicinity of sunspots towards the end of their existence.

Methods. We present a subset of multi-wavelengths observations obtained with the Japanese *Hinode* mission, the *Solar Dynamics Observatory* (SDO), and the *Vacuum Tower Telescope* (VTT) at *Observatorio del Teide*, Tenerife, Spain during the time period from 2010 November 18–23. Horizontal proper motions were derived from G-band and Ca II H images, whereas line-of-sight velocities were extracted from VTT Echelle H α λ 656.28 nm spectra and Fe I λ 630.25 nm spectral data of the *Hinode/Spectro-Polarimeter*, which also provided three-dimensional magnetic field information. The *Helioseismic and Magnetic Imager* on board SDO provided continuum images and line-of-sight magnetograms as context for the high-resolution observations for the entire disk passage of the active region.

Results. We have performed a quantitative study of photospheric and chromospheric flow fields in and around decaying sunspots. In one of the trailing sunspots of active region NOAA 11126, we observed moat flow and moving magnetic features (MMFs), even after its penumbra had decayed. We also noticed a superpenumbral structure around this pore. MMFs follow well-defined, radial paths from the spot all the way to the border of a supergranular cell surrounding the spot. In contrast, flux emergence near the other sunspot prevented it from establishing such well ordered flow patterns, which could even be observed around a tiny pore of just 2 Mm diameter. After the disappearance of the sunspots/pores a coherent patch of abnormal granulation remained at their location, which was characterized by more uniform horizontal proper motions, low divergence values, and diminished photospheric Doppler velocities. This region, thus, differs significantly from granulation and other areas covered by G-band bright points. We conclude that this peculiar flow pattern is a signature of sunspot decay and the dispersal of magnetic flux.

Key words. Sun: chromosphere – Sun: photosphere – Sun: surface magnetism – Sun: sunspots – Techniques: image processing – Methods: data analysis

1. Introduction

Sunspots are a thought-provoking aspect of solar activity because of the close interaction between plasma motions and magnetic fields. Recent progress in MHD simulations (e.g., Rempel, 2011) provide a comprehensive framework for the interpretation of high-resolution sunspot observations. The formation of a penumbra around a sunspot is a rapid phenomenon, i.e., within a few hours a sunspot can develop a penumbra (Leka & Skumanich, 1998; Yang et al., 2003), which is intimately linked to more inclined magnetic field lines and the onset of the Evershed flow. Schlichenmaier et al. (2010) observed the growth of a penumbra where only the newly formed penumbra contributed to the increase in spot size while the umbra remained stable. The formation of a penumbra, which would surround the

entire spot, was hindered by continuous flux emergence between the spots of the bipolar region.

Quite the opposite, the decay of a sunspot is a slow process. Decay rates for stable leading sunspots and irregular follower spots are different (Martínez Pillet, 2002). A number of decay laws were proposed such as a linear decay law described by Bumba (1963) and a parabolic decay law proposed by Petrovay & van Driel-Gesztelyi (1997). Martínez Pillet (2002) critically reviews various diffusion models, concludes that they explain well how flux is spread over larger areas while the spot is decaying, but they fail to satisfactorily describe the flux removal process. The initial stages of sunspot decay, i.e., when the spot loses its penumbra, are exemplarily described in Bellot Rubio et al. (2008), who discovered finger-like structures, which are neither related to penumbral filaments nor the Evershed flow.

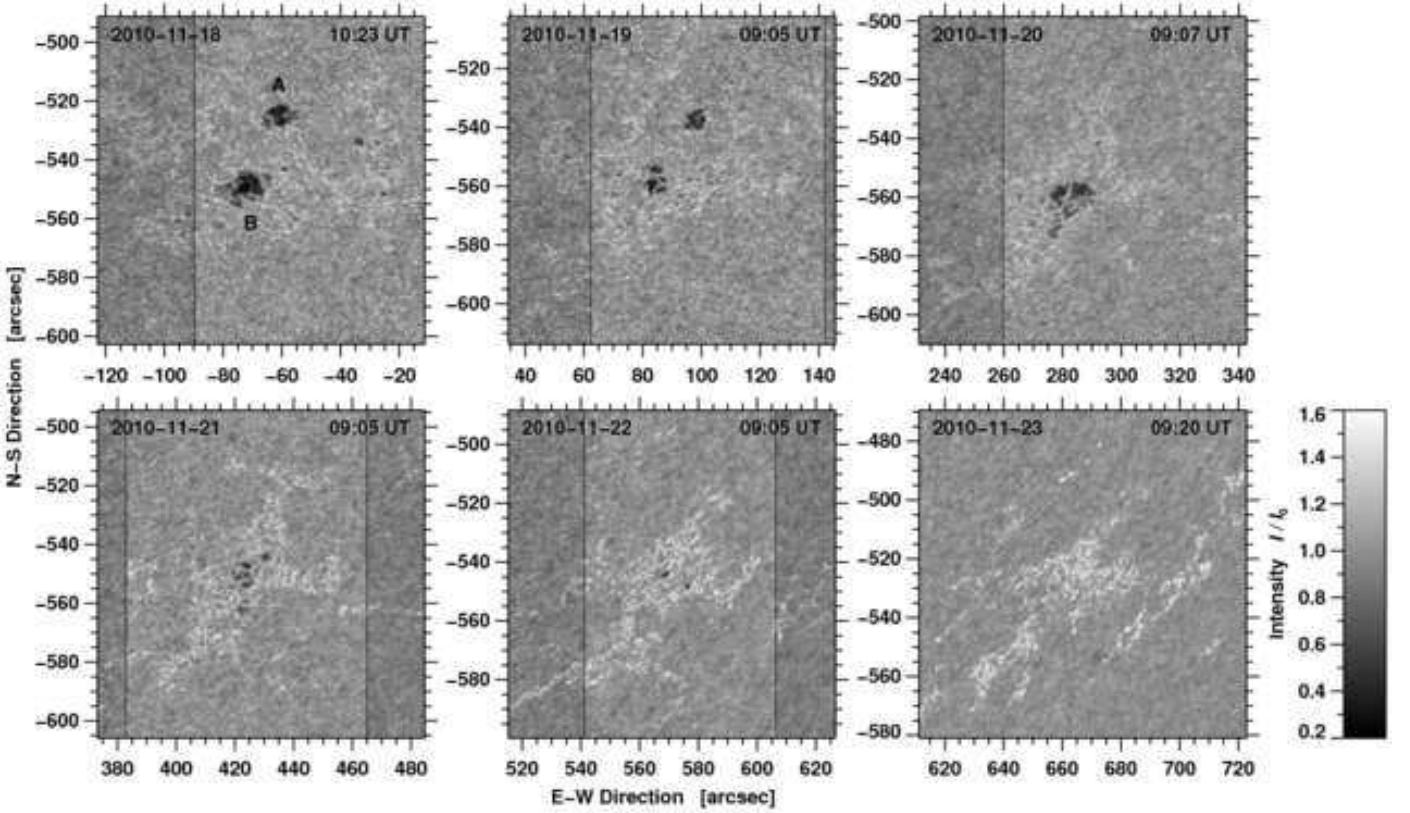


Fig. 1. Calibrated *Hinode* G-band images showing the decay of active region NOAA 11126 observed during the period from 2010 November 18–23 (from top-left to bottom-right). The FOV is $111'' \times 111''$. The annotation of the axes refers to heliocentric coordinates given in seconds of arc. Brighter areas delineated by vertical black lines correspond to regions, which were covered by spectral scans obtained with the VTT Echelle spectrograph. The intensity scale to the right applies to these regions, while areas not covered by Echelle data are displayed with an offset of $0.1I_0$. On 2010 November 23, only few *Hinode* G-band images were available. The limb darkening has been subtracted from the G-band images, which were then normalized so that the mean of the quiet Sun intensity distribution corresponds to unity.

These features might be penumbral field lines rising to the chromosphere, thus contributing to the decay of the sunspot penumbra. When a sunspot loses its penumbra, its decay reaches a critical point. Magnetic field lines become more vertical and convective motions in its vicinity begin to change. These ideas of a critical inclination angle and convective motions were put together by Rucklidge et al. (1995), who explains in a simple model why small sunspots can have a penumbra while larger pores do not possess one.

The moat flow is a large-scale flow pattern commonly observed around sunspots (Meyer et al., 1974). However, flux removal and dispersal can only be understood in the context of the moat flow’s fine structure. Moving magnetic features (MMFs) play a major role in the flux dispersal process and they are only associated with decaying sunspots (Harvey & Harvey, 1973). The total flux carried by MMFs is several times larger than the flux contained within the sunspot itself. Thus, the polarity of MMFs has to be considered for a balance of the net flux. MMFs move radially outward with a velocity of 1 km s^{-1} before they reach and dissolve within the network, i.e., at the boundaries of the supergranular cell containing the sunspot. Zuccarello et al. (2009) showed evidence that MMFs and moat flow are present even in the vicinity of pores, i.e., in the absence of penumbral filaments and Evershed flow (cf., Cabrera Solana et al., 2006). Deng et al. (2007) also detected a persistent moat flow after the penumbra around spot disappeared leaving only a pore. Even

though the moat flow might not be closely tied to the Evershed flow, the sub-photospheric interaction of magnetic field lines and flows can still produce the observed flow patterns.

Verma & Denker (2011) described a local correlation tracking (LCT) method to measure horizontal flows based on *Hinode* G-band images. In this study, we perform a case study, where we put such horizontal flow fields in the context of other photospheric and chromospheric data. In particular, we are interested in the final stages of sunspot decay. In Sect. 2, we present a subset of multi-wavelengths observations, which were obtained within the scope of *Hinode* Operation Plan (HOP) 0176. The temporal evolution of active region NOAA 11126 in terms of intensity, morphology, and flow as well as magnetic fields is described in Sect. 3 and discussed in Sect. 4.

2. Observations

The disk passage of active region NOAA 11126 started on 2010 November 12 and ended on November 24. NOAA 11126 was classified as a β -region, while it crossed the solar disk. No major flaring was associated with the region. Only a few B-class events were reported on 2010 November 15. As part of HOP 0176 “*High-resolution multi-wavelength study of small-scale jets on the solar disk*”, we observed the decay of two small follower sunspots in the active region for five days from 2010 November 18–22. A time-series of *Hinode* G-band images is shown in

Table 1. Observing characteristics and physical parameters

November		18	19	20	21	22
B		S32.6°	S32.6°	S32.6°	S32.6°	S32.6°
L		E5.5°	W6.3°	W20.5°	W31.5°	W44.1°
μ		0.81	0.81	0.77	0.70	0.58
$t_{0,GB}$	UT	10:23	09:05	09:07	09:05	09:05
$t_{0,SP}$	UT	11:46	09:05	09:07	09:04	09:04
$t_{0,ES}$	UT	10:22	08:59	14:16	09:31	08:47
$A_{Spot\ A}$	Mm ²	33.8	21.5			
$v_{Spot\ A}$	km s ⁻¹	0.22 ± 0.19	0.15 ± 0.15			
		0.20 ± 0.25	0.15 ± 0.14			
$v_{Ring\ A}$	km s ⁻¹	0.44 ± 0.23	0.37 ± 0.19			
		0.44 ± 0.23	0.38 ± 0.19			
$ \nabla v _{Ring\ A}$	10 ⁻³ s ⁻¹	0.83 ± 0.78	0.65 ± 0.54			
		1.28 ± 1.33	1.13 ± 1.06			
$A_{Spot\ B}$	Mm ²	54.7	21.6	54.2	17.5	2.7
$v_{Spot\ B}$	km s ⁻¹	0.22 ± 0.15	0.15 ± 0.15	0.16 ± 0.07	0.18 ± 0.05	0.28 ± 0.06
		0.20 ± 0.14	0.11 ± 0.05	0.15 ± 0.08	0.25 ± 0.06	0.37 ± 0.06
$v_{Ring\ B}$	km s ⁻¹	0.31 ± 0.19	0.20 ± 0.12	0.28 ± 0.14	0.25 ± 0.14	0.30 ± 0.09
		0.32 ± 0.20	0.20 ± 0.12	0.29 ± 0.15	0.28 ± 0.13	0.40 ± 0.09
$ \nabla v _{Ring\ B}$	10 ⁻³ s ⁻¹	0.63 ± 0.68	0.37 ± 0.36	0.46 ± 0.49	0.47 ± 0.51	0.28 ± 0.33
		0.91 ± 1.20	0.47 ± 0.59	0.76 ± 1.04	0.63 ± 0.81	0.44 ± 0.44
A_{mag}	Mm ²	136.9	83.5	98.9	44.7	22.2
N_{mag}		10	5	9	6	2
v_{mag}	km s ⁻¹	0.22 ± 0.12	0.15 ± 0.09	0.16 ± 0.07	0.18 ± 0.05	0.28 ± 0.06
v_{bp}	km s ⁻¹	0.27 ± 0.19	0.27 ± 0.16	0.28 ± 0.16	0.23 ± 0.12	0.26 ± 0.10
v_{gran}	km s ⁻¹	0.40 ± 0.24	0.35 ± 0.20	0.37 ± 0.20	0.34 ± 0.19	0.34 ± 0.18
$ \nabla v _{gran}$	10 ⁻³ s ⁻¹	0.88 ± 0.89	0.72 ± 0.67	0.85 ± 0.79	0.95 ± 0.88	1.04 ± 0.98
$ v _{mag,LOS}$	km s ⁻¹	0.03 ± 0.17	0.02 ± 0.12	0.04 ± 0.20	0.02 ± 0.12	0.00 ± 0.02
$ v _{bp,LOS}$	km s ⁻¹	0.43 ± 0.37	0.44 ± 0.37	0.44 ± 0.38	0.41 ± 0.38	0.34 ± 0.30
$ v _{gran,LOS}$	km s ⁻¹	0.51 ± 0.41	0.50 ± 0.41	0.55 ± 0.45	0.57 ± 0.47	0.55 ± 0.45

The parameters in the first column of the table refer to heliographic latitude B , heliographic longitude L , cosine of the heliocentric angle μ , start of the G-band (GB), spectro-polarimeter (SP), and Echelle spectrograph (ES) observing sequences t_0 , spot area A , horizontal velocity v , mean divergence $|\nabla v|$, number of magnetic elements N_{mag} . The indices refer to G-band bright points (bp), granulation (gran), magnetic elements (mag), the two sunspots (Spot A and Spot B), and the four-megameter wide annuli around both spots (Ring A and Ring B). If two rows are given for a physical parameter, then the top row refers to G-band data, whereas the bottom row was derived from Ca II H data. If present, the standard deviation refers to the variation of the physical parameters within the specified regions rather than to any formal error.

Fig. 1, where we labeled the northern and southern spots with A and B, respectively. In the following, we will simply refer to these magnetic features as *spots*, even if the proper classification should be *pores*, i.e., sunspots lacking a penumbra. Spectral scans with different field-of-views (FOVs) and cadences were observed for three hours every day. Since we are only focusing on the general properties of sunspot decay, we chose the first scan on the given day, which covered the largest FOV. The settings for the *Vacuum Tower Telescope* (VTT) Echelle data and data of *Hinode/Spectro-Polarimeter* were chosen as to obtain the best spatial and spectral match. The general observing characteristics are listed in Tab. 1.

2.1. SDO/HMI full-disk images

The discussion of the temporal evolution and morphology of active region NOAA 11126 is based on full-disk images and line-of-sight (LOS) magnetograms obtained with the *Helioseismic and Magnetic Imager* (HMI, Schou et al., 2010; Couvidat et al., 2011; Wachter et al., 2011) on board the *Solar Dynamics Observatory* (SDO). Since the *Hinode* FOV is too small to cover the entire active region and to give an overview of the magnetic field topology, we show in Fig. 2 the limb-darkening corrected HMI continuum image and magnetogram for November 18.

We selected from the SDO/HMI database one image/magnetogram with 4096×4096 pixels every 15 min for the period from 2010 November 13–23, i.e., a total of 1056 full-disk images. The image scale is about $0.5'' \text{ pixel}^{-1}$, so that even finer details of penumbra and umbra can be captured. The average limb-darkening function was computed for this time interval and subtracted from the full-disk images to yield contrast enhanced images (see e.g., Denker et al., 1999), which can then be

used for feature identification. The photometric temporal evolution for the entire active region as shown in Fig. 2 is depicted in Fig. 3. The corresponding changes of the magnetic flux are shown in Fig. 4. Since HMI data cover the whole solar disk, it is straightforward to compute the heliocentric angle μ on a pixel-by-pixel basis. Thus, a geometrical correction is applied to the measured areas and flux values of Figs. 3 and 4, which are discussed in detail in Sects. 3.1 and 3.5, respectively.

2.2. *Hinode* G-band and Ca II H images

We applied LCT (for details see Verma & Denker, 2011) to image sequences captured in G-band $\lambda 430.5 \text{ nm}$ and Ca II H $\lambda 396.8 \text{ nm}$ to compare horizontal flows in the photosphere and chromosphere. Note that the Ca II H images do not purely represent the chromosphere, but contain contributions from both the upper photosphere and lower chromosphere. These observations were carried out by the *Broad-band Filter Imager* (BFI) of the *Solar Optical Telescope* (SOT, Tsuneta et al., 2008) on board *Hinode* (Kosugi et al., 2007). Data sequences were captured every day from 09:00 UT to 12:00 UT with an average time cadence of 120 s (with some jumps in the data sequences). In both wavelengths the images are 2×2 -pixel binned with an image scale of $0.11'' \text{ pixel}^{-1}$. Images have a size of 1024×1024 pixels and a FOV of $111'' \times 111''$.

After basic data calibration, the images were corrected for geometrical foreshortening and resampled onto a regular grid of $80 \text{ km} \times 80 \text{ km}$. The signature of the five-minute oscillation was removed from the images by using a three-dimensional Fourier filter with a cut-off velocity of 8 km s^{-1} corresponding roughly to the photospheric sound speed. For measuring horizontal proper motions, we applied the LCT algorithm described in Verma &

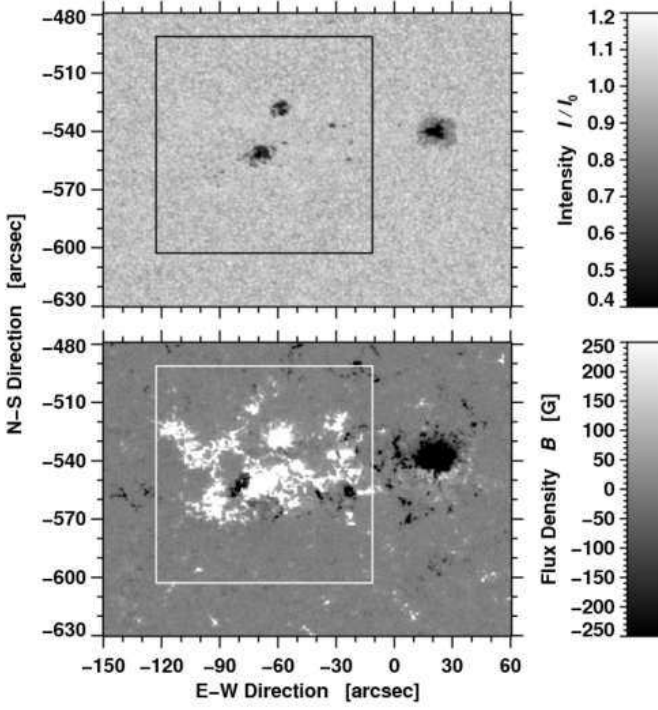


Fig. 2. Limb-darkening corrected HMI continuum image (*top*) and magnetogram (*bottom*) of active region NOAA 11126 on November 18. The square box in both images shows the FOV covered by *Hinode*/BFI. The axes are labeled in heliographic coordinates.

Denker (2011), which computes cross-correlations over 32×32 -pixel regions with a Gaussian kernel having a FWHM of 15 pixels (1200 km) corresponding to the typical size of a granule. In two aspects we deviated from the aforementioned algorithm, the time cadence was $\Delta t = 120$ s and the flow maps were averaged over $\Delta T = 3$ h.

2.3. $H\alpha$ Echelle spectra

The observations in $H\alpha$ $\lambda 656.28$ nm and Fe I $\lambda 656.92$ nm were carried out with the VTT Echelle spectrograph. Spectral data were acquired with a slit width of $80 \mu\text{m}$ and an exposure time of 300 ms. The image-scale of the spectrograph is $8.99'' \text{mm}^{-1}$. We did not use a predisperser, hence, to suppress overlapping in spectral orders, we placed a broad-band interference filter directly behind the spectrograph slit. The infrared grating with a blaze angle of 51.6° and 200 grooves mm^{-1} was used to record spectra in the 12th order. In this configuration, we achieved a dispersion of $0.60 \text{ pm pixel}^{-1}$. The spectra covered a wavelength range of 1.2 nm from $\lambda 655.9$ nm to $\lambda 657.1$ nm. We employed a PCO.4000 CCD camera that has a quantum efficiency of about 30% at $H\alpha$. After 2×2 -pixel binning the images have a size of 2004×1336 pixels. The pixel size of the CCD detector is $9 \mu\text{m} \times 9 \mu\text{m}$. The Echelle data were intended to match the *Hinode* observations, which was mostly achieved except for a few interruptions because of deteriorating seeing conditions. The two-dimensional FOV was scanned with a spatial step of $0.32''$ and 200–250 spectra were recorded in a sequence. A sequence of 240 spatial steps took about 12 min and covered a FOV of $72.0'' \times 182.6''$.

The common FOVs of the G-band images and $H\alpha$ Echelle spectra are shown in Fig. 1 for each observing day. We first

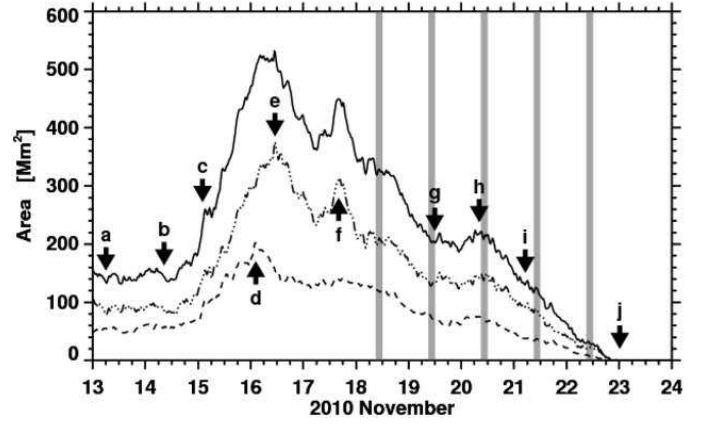


Fig. 3. Temporal evolution of the area covered by active region NOAA 11126 while it crossed the solar disk. The area enclosed by umbral cores and pores is displayed with dashed line. Dashed dot dot line refers to the penumbra, whereas solid line denotes the total area. Some smoothing was applied to the time-series to suppress features on temporal scales below one hour. The vertical gray bars refer to the observing periods of HOP 0176 (2010 November 18–22). The labels indicate different stages of active region evolution, which are explained in Sect. 3.1.

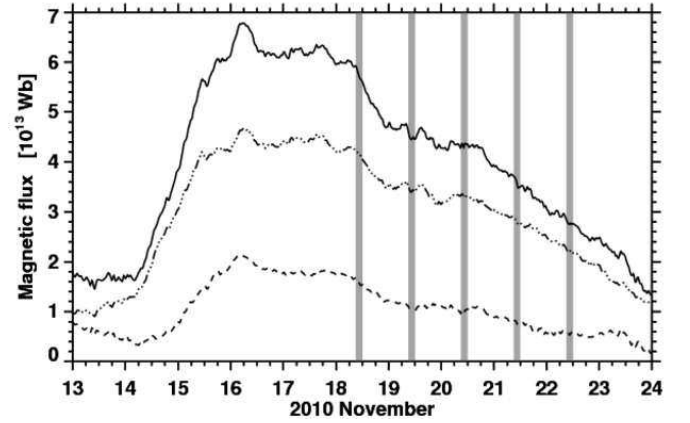


Fig. 4. Temporal evolution of the magnetic flux contained in active region NOAA 11126 while it crossed the solar disk. The solid, dashed dot dot, and dashed lines refer to the total, positive, and negative flux, respectively.

matched the image scale of the Echelle data to that of the *Hinode* data. We then aligned *Hinode* G-band images and continuum images derived from Echelle spectra. After this procedure, the heliocentric coordinates for G-band images and $H\alpha$ spectra differ by less than $1''$ in the periphery of the FOV. Furthermore, the Echelle scan direction is not perfectly aligned with the *Hinode* BFI detector. Hence, we computed an offset angle (smaller than $\pm 2^\circ$) for each date and applied it to the spectral data. On 2010 November 20, the time difference between G-band images and Echelle spectra was about five hours.

2.4. *Hinode* Spectro-Polarimeter

The photospheric magnetic topology and evolution of the active region were studied using high-resolution spectral data from the *Hinode*/Spectro-Polarimeter (SP, Ichimoto et al., 2008), which uses two magnetically sensitive Fe I lines at $\lambda 630.15$ nm and $\lambda 630.25$ nm and the nearby continuum (Tsuneta et al., 2008)

to obtain Stokes *IQUV* spectral profiles. We used spectral data captured in the fast mapping mode with a FOV of $58'' \times 122''$ and an average scan time of 12 min. On November 18, we also used ten continuous high cadence scans with a FOV of $32'' \times 123''$ and a scan time of 7 min. The dispersion is about $2.155 \text{ pm pixel}^{-1}$. The region was scanned with a spatial step of about $0.3''$ and image scale of $0.32'' \text{ pixel}^{-1}$. The basic data reductions such as subtraction of dark current, flat fielding, polarization, and wavelength correction were performed using procedures available in SolarSoft (SSW, Bentley & Freeland, 1998; Freeland & Handy, 1998).

3. Results

3.1. Photospheric evolution

Contrast-enhanced HMI full-disk continuum images were used to study the evolution and decay of active region NOAA 11126 during its disk passage. The curves in Fig. 3 correspond to the areas of umbral cores/pores, penumbrae, and the sum of both types of features. These strong magnetic features are identified according to intensity thresholds of 75% and 92%, respectively, where the quiet Sun intensity was normalized to unity. Some spatial smoothing and minimum-size criteria were applied to binary masks of identified features using morphological image processing techniques, thus ensuring unwrinkled boundaries and contiguous structures. Note that this algorithm only provides a rough estimate of the above areas. Some (small) features could be misclassified. In particular, the borders of pores will be classified as penumbra.

The most important stages of the active region evolution are labeled in Fig. 3: (a) Initially, two tightly spaced sunspots of positive polarity were present early on November 13. The leading spot was larger and had a well established penumbra. (b) New flux emerged towards the south-east of these spots at 8:30 UT on November 14. Numerous (more than ten) magnetic knots and pores appeared to the south-west forming a bipolar magnetic region. (c) The umbral core of leading sunspot of the new group established at 2:00 UT on November 15. (d) The leading sunspot of the new group continuously grew by advecting magnetic knots and small pores. The umbral cores/pores occupied the largest area at 2:20 UT on November 16. (e) The penumbra of the leading spot reached its maximum about nine hours later. At this time, the active region NOAA 11126 started its decay phase. (f) Some further flux emergence occurred in the trailing part of the region at about 16:00 UT on November 17, which strengthened spot B and produced thin elongated dark lanes. These typical features of flux emergence (see e.g., Strous et al., 1996) were labeled erroneously as penumbrae by the thresholding algorithm.

HOP 0176 focused on the two trailing spots/pores, of which the northern one (spot A) was already decaying, while the southern one (spot B) had just reached its maximum. This sunspot also showed strong indications of rotation. (g) This spot then fragmented into numerous magnetic knots until about 19:30 UT on November 19. (h) At this time, the fragments started to converge again forming a small sunspot, which reached its maximum at 8:00 UT on November 20. Interestingly, the northern pore faded away in parallel to this growth spurt. (i) Most of the penumbra in the leading spot has disappeared by 5:00 UT on November 21. (j) Finally, on November 23, all spots, pores, and magnetic knots had vanished and only a bright plage region remained until it rotated off the visible hemisphere.

In summary and neglecting all details of active region evolution, active region decay rates can be computed using a linear fit

for time periods when the area coverage reached its maximum to the point when the area fell below 5 Mm^2 . The overall decay rate of the active region is 72.6 Mm^2 per day. The values for penumbrae and umbral cores/pores are 48.3 and 25.1 Mm^2 per day, respectively. Similarly, we computed the growth rate of umbrae and penumbrae starting at 21:00 UT on November 14. The values are 171.4 and 104.8 Mm^2 per day, respectively. This is about four times faster than the corresponding decay times but less than one half of the penumbral growth rate of about 400 Mm^2 per day presented by Schlichenmaier et al. (2010).

Hinode G-band images allow us to zoom in on the two trailing spots. The region-of-interest (ROI) is shown in the top row of Fig. 5. The data of 2010 November 18–22 are corrected for geometrical foreshortening and the center-to-limb variation. The ROI with a size of 756×756 pixels or $60 \text{ Mm} \times 60 \text{ Mm}$ was centered at a heliographic latitude of $S31.9^\circ$. The first G-band image of the daily observing sequences was used as a reference to align all other data.

Various solar features are identified using intensity thresholds and morphological image processing. We indiscriminately used a fixed intensity threshold of $I_{\text{mag}} = 0.8I_0$ for strong magnetic features and an adaptive threshold for G-band bright points of $I_{\text{bp}} = (1.37 - 0.08\mu)I_0$, where μ is the cosine of the heliocentric angle θ , and I_0 refers to the average quiet Sun intensity. Intensity values between I_{bp} and I_{mag} consequently enclose granulation. The measured spot areas for HMI and *Hinode* agree with each other, and the remaining differences can be attributed to different spectral characteristics of the observed passbands, image scales, and threshold/selection criteria. In general, the temporal evolution within the ROI follows the same trend as discussed in the context of SDO observations (Fig. 3). Areas, velocities, and other physical quantities based on high-resolution data are included in Tab. 1.

In the following, we present a chronology of the important phases of sunspot decay based on the high-spatial resolution G-band images. On November 18, the two trailing sunspots were embedded in a network of G-band bright points hinting at widely dispersed, weak magnetic fields. Both spots were filled with numerous umbral dots. Spot A had three umbral cores separated by faint light bridges and a small penumbral segment pointing westward. Spot B had two umbral cores with a few associated magnetic knots. It possessed curved penumbral filaments pointing eastwards, which are indicative of twisted magnetic field lines. These kind of non-radial penumbral filaments are frequently observed in flaring sunspots with horizontal shear flows (Denker et al., 2007; Deng et al., 2006). On November 19, the faint light-bridges had disappeared and the penumbra had vanished leaving only a single pore, which was filled with conglomerates of umbral dots. Spot B also lost its penumbra leaving four umbral cores separated by faint light-bridges, which, however, were more pronounced in comparison to previous day. Magnetic knots were still surrounding spot B. Spot A had decayed on November 20 with only two faint magnetic knots remaining at its location. Interestingly, at this point of time spot B started to grow in area with hints of penumbral filament being visible on its western side. It consisted of three umbral cores, which were now separated by strong light-bridges, which split the spot in two halves along its north-south axis. The presence of strong light-bridges might suggest the initiation of the spot's decay phase (see Sobotka et al., 1993). Once spot A had disappeared on November 21, it did not leave any significant trace within the network of G-band bright points. By this time spot B had dissolved into multiple tiny pores and magnetic knots, which roughly covered the same region as on the previous day. By

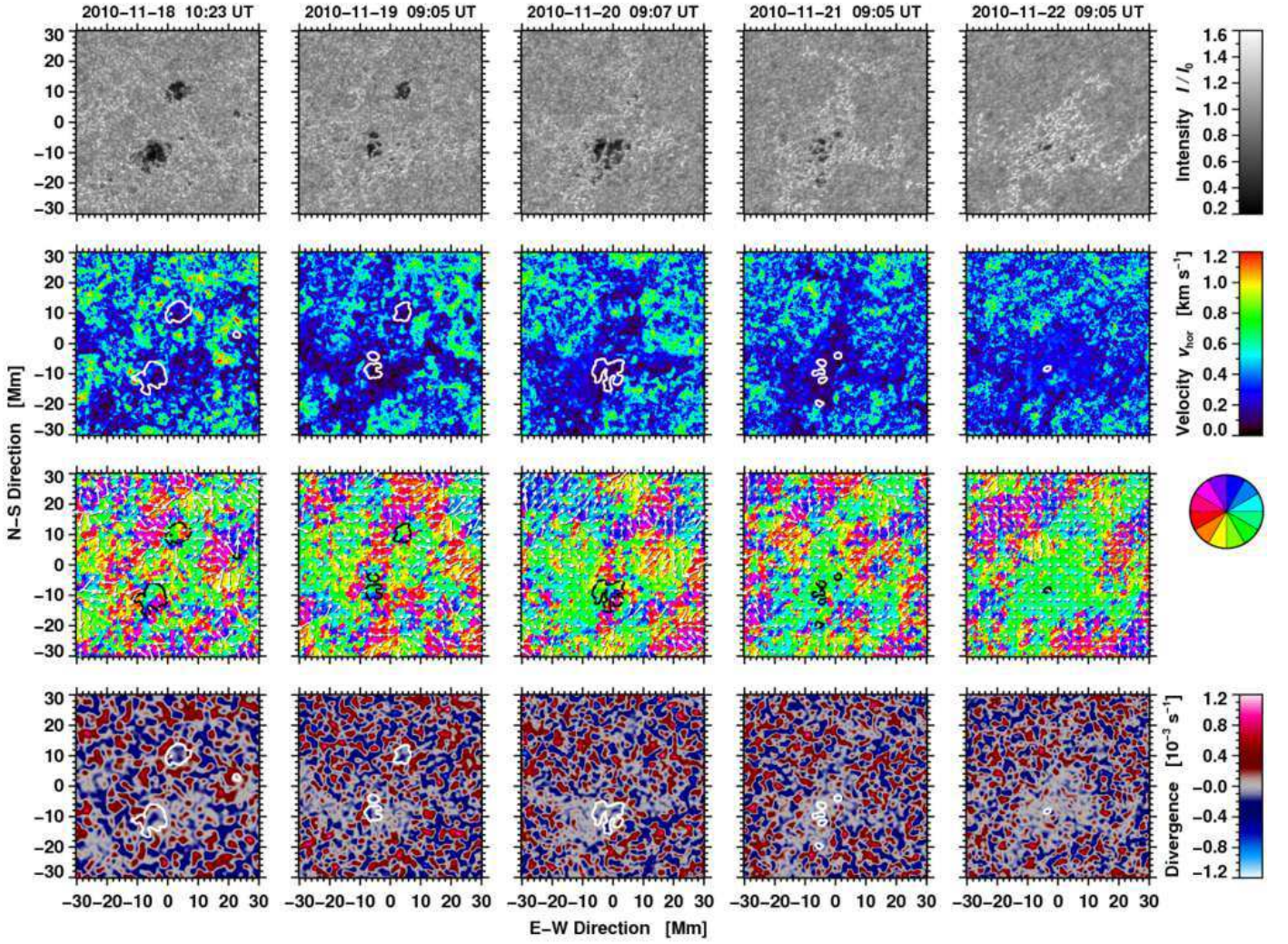


Fig. 5. G-band images (*top*) after correction of geometrical foreshortening tracing the photospheric evolution of the central part of active region NOAA 11126 (from left to right 2010 November 18–22). The horizontal flow speeds (*2nd row*) are given by the velocity scale to the right. The direction of the horizontal flows (*3rd row*) are displayed according to the color-wheel and arrows for which a velocity of 1 km s^{-1} corresponds to exactly the grid spacing. The divergence of the horizontal flow field (*bottom*) are presented according to the scale on the right, where gray indicates divergence values close to zero. All G-band images and LCT maps were aligned so that the center of the panels coincides with a latitude of 31.9° South. The white and black contours outline the location of the small sunspot/pores. Times refer to the first image of the time-series, which was used to compute the flow maps.

November 22, only two tiny pores were left from spot B, which disappeared on November 23 just leaving G-band bright points at its point of disappearance. Two observations are noteworthy: (1) The area covered by the G-band bright points remained almost constant during the disk passage of the active region, which suggests that flux decays more or less in place and is not redistributed over a larger area. The time scale of flux removal or dispersal extends well beyond the photometric decay time of strong magnetic features such as sunspots, pores, and magnetic knots. (2) The two trailing spots have different histories of flux emergence and decay.

3.2. Chromospheric evolution

The description of the chromospheric evolution is based on Ca II H (top row of Fig. 6) and H α line core intensity maps (top row of Fig. 8). The Ca II H images were averaged over three hours to highlight some of the long-lived chromospheric features. On November 18, the lower quarter of the Ca II H image

showed the undisturbed pattern of inverse granulation (Rutten et al., 2004). Ca II H brightenings cover a larger area, since their filling factor is significantly greater than that of G-band bright points. Spot A was encircled by individual brightenings at a radial distance of 5 Mm. These individual brightenings coalesced into a wagon-wheel-like Ca II H intensity structure in the three-hour average image pointing to the presence of MMFs. A similar feature was noticeable around a much smaller pore with a diameter of about 2 Mm located to the west of spot A. This conspicuous Ca II intensity structure was first described by Shine et al. (1996), who identified the bright ridges with azimuthal convergence regions, whereas the dark regions between the spokes correspond to azimuthal divergence zones. Spot A resides in the middle of a supergranular cell with a diameter of about 20 Mm. In contrast, spot B is embedded in an area of much more pronounced Ca II H brightenings. The exterior tips of its penumbral filaments appeared bright because a low-level B-class flare occurred at the time of observations.

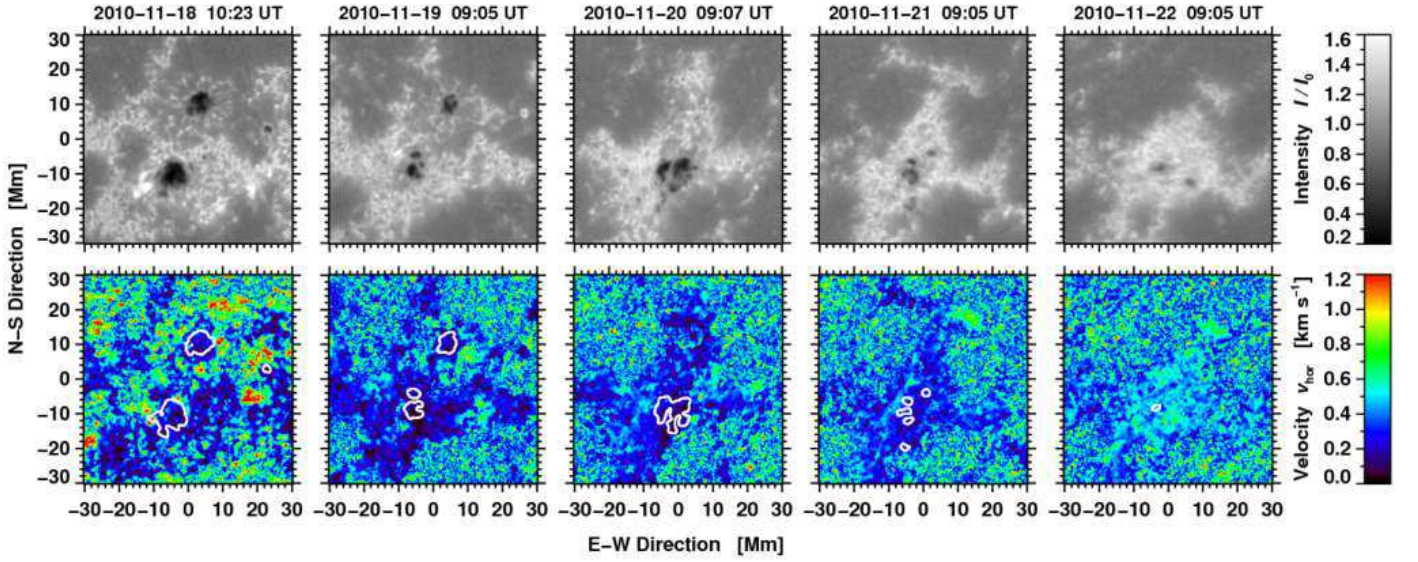


Fig. 6. Ca II H average images tracing the evolution of active region NOAA 11126 in the chromosphere. The horizontal proper motions were derived from time-sequences of Ca II H images. Otherwise, data processing and display are the same as in Fig. 5.

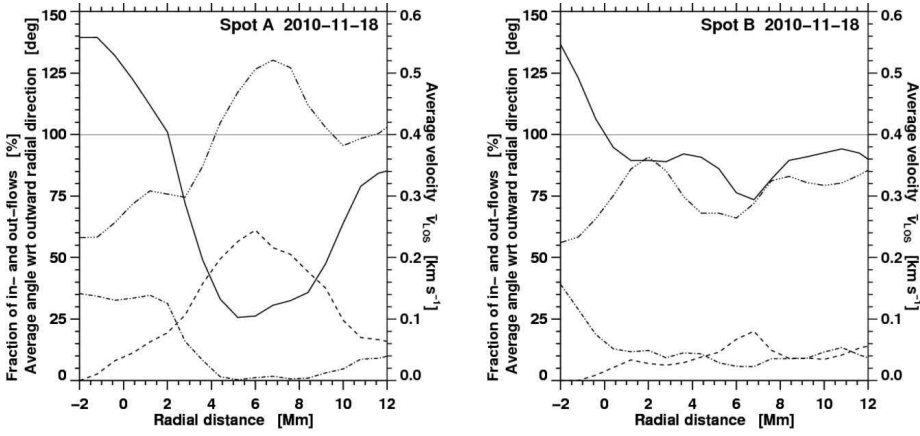


Fig. 7. Radial dependence of parameters characterizing the flow fields of spots A (left) and B (right). Radial distances are measured from the outer boundary of the spots, i.e., 0.0 Mm marks the transition from penumbra to granulation. The thick black curves indicate the average angle of horizontal flow vectors with respect to the outward radial direction. High values refer to inward flows and low values indicate outward flow vectors. Fractions of in-/outward flow vectors as defined in the text are shown as a dash-dotted and dashed lines, respectively. The horizontal straight line denotes the 100%-level. The average flow speed is displayed as a dash-dot-dot-dotted line.

On November 19, the average Ca II H image showed evidence that the moat flow around spot A survived the initial stages of sunspot decay, even after its penumbra had disappeared (see e.g., Deng et al., 2007). Spot A had completely dissolved by November 20. Assuming that spot A was located in the center of a supergranular cell as indicated by the surrounding Ca II H brightenings on November 18 and 19, we conclude that this supergranular cell ceased to exist on November 20, when the strong magnetic fields of spot A were no longer present. The Ca II H brightenings are now squeezed together by two supergranular cells to east and to the west, which could already be identified on November 19 and remained visible until November 22.

At the time when spot A vanished, spot B had already fragmented into two umbral cores, which were separated by a strong light-bridge with a noticeable dark lane along its axis (Rouppé van der Voort et al., 2010). This dark core was even more clearly discernible in the three-hour average Ca II H image. The presence of strong light-bridge can be taken as a first indication of the spot entering the decay phase. During the next two days on November 21–22, spot B decayed further.

The H α line core intensity map of November 18 exposed a radial pattern of fibrils around spot A reminiscent of a super-penumbra. Strong brightenings in the H α line core in the vicinity

of spot B are related to the aforementioned small B-class flare. We did not notice any significant H α intensity features on the following days, except that after the decay of both spots the H α plage became more prominent. By the end of our observations with the Echelle spectrograph, only a very compact plage region with a length of about 8 Mm remained within ROI.

3.3. Horizontal proper motions

The LCT flow maps displayed in Figs. 5 and 6 were computed using the time-sequence of *Hinode* G-band and Ca II H images. As mentioned in Section 3.1, we distinguished various solar features (e.g., G-band bright points, granulation, strong magnetic features, and sunspot penumbrae) by morphological and adaptive thresholding. For comparison, we refer to the typical flow speeds of granulation $v_{\text{gran}} = 0.47 \pm 0.27 \text{ km s}^{-1}$ and G-band bright points $v_{\text{bp}} = 0.23 \pm 0.15 \text{ km s}^{-1}$ as reported by Verma & Denker (2011), who also presented values for longer time intervals ΔT (Tab. 1 therein) and cadences Δt (Fig. 3 therein). Their values for granulation are in very good agreement with the mean values $\bar{v}_{\text{gran}} = 0.36 \pm 0.20 \text{ km s}^{-1}$ of the present study. The mean values for bright points $\bar{v}_{\text{bp}} = 0.26 \pm 0.15 \text{ km s}^{-1}$ in the neighborhood of active region NOAA 11126 are within the range of expected values. Daily values of flow speeds for granulation and

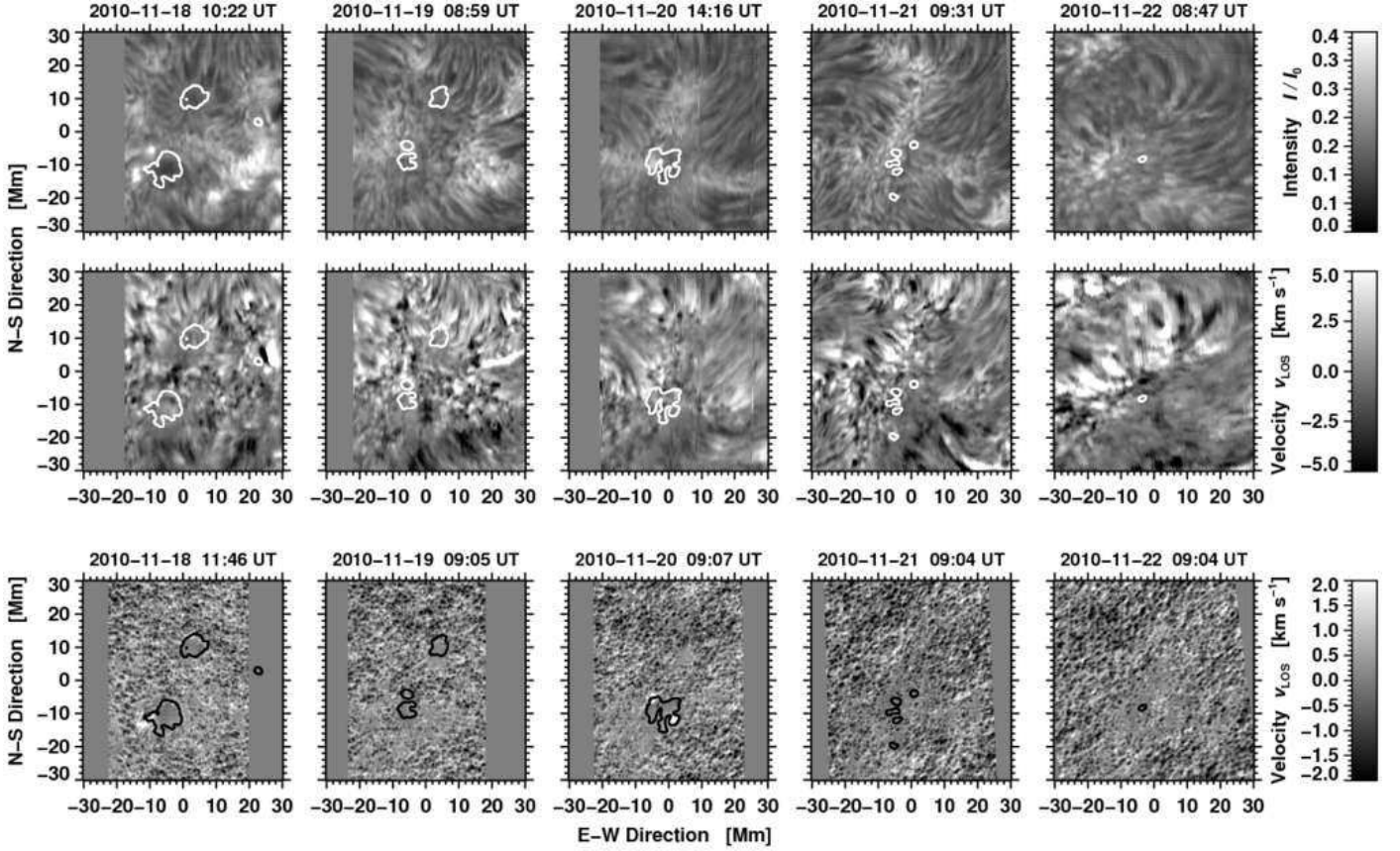


Fig. 8. VTT Echelle spectra were used to study the chromospheric evolution of active region NOAA 11126 during the period from 2010 November 18–22. The chromospheric fibril structure surrounding the decaying sunspots can be traced in $H\alpha$ $\lambda 656.28$ nm line core intensity (*top*) and LOS velocity (*middle*) maps. In addition, photospheric LOS velocities (*bottom*) were derived from *Hinode*/SP Fe I $\lambda 630.25$ nm spectra. The FOV matches those of Figs. 5 and 6. Regions not covered by the spectral data are shown in medium gray. The times above the panels refers to the start of a spectral scan.

G-band bright points are given in Tab. 1. The standard deviation of the aforementioned horizontal flow speeds refers to the variance in the data for a particular solar feature rather than to a formal error. The intrinsic error of the LCT algorithm is 50 m s^{-1} and 15° for flow speed and direction, respectively (see Verma & Denker, 2011).

We computed the flow vectors for strong magnetic elements, i.e., spots A and B. We identified spots by smoothing the geometrically corrected G-band images using a Gaussian kernel with a FWHM of 1280 km and subsequently applied an intensity threshold of $0.83I_0$. We plotted contours based on these binary masks in Figs. 5 and 6 to provide some visual guidance in identifying the spot positions in the physical maps. The mean flow speeds $\bar{v}_{\text{Spot A}} = 0.19 \pm 0.17 \text{ km s}^{-1}$ and $\bar{v}_{\text{Spot B}} = 0.18 \pm 0.11 \text{ km s}^{-1}$ are virtually identical for both spots. While computing the mean velocity $\bar{v}_{\text{Spot B}}$ for spot B, we discarded November 22, because on that day only a tiny pore with a diameter of 4 Mm was left at the location of spot B. Therefore, adjacent regions with G-band bright points and granulation would bias the flow speed towards higher values. The overall flow pattern for the Ca II H data is very similar as compared to G-band data, and the average values $\bar{v}_{\text{Spot A}} = 0.18 \pm 0.20 \text{ km s}^{-1}$ and $\bar{v}_{\text{Spot B}} = 0.18 \pm 0.08 \text{ km s}^{-1}$ are virtually identical with a tendency to be slightly lower on individual days.

The moat flow around sunspots and pores reveals itself as radially, outward-directed vectors in flow maps, which point to

a ring-like structure with kernels of elevated flow speeds. In the speed and azimuth maps on November 18 and 19 (Figs. 5 and 6) indications of moat flow were visible around spot A and a small pore located to the west of spot A. There was no clear signature of the moat flow detectable around spot B. To express the characteristics of the moat flow in more quantitative terms, we plotted in Fig. 7 the angle of the flow vectors, the fraction of in- and outward flow vectors, and the horizontal velocities for spots A and B. These quantities are radial averages and the zero point of the radial distance was placed at the penumbra/granulation boundary of the spots. We considered a flow vector to point in-/outward, if the tip of the arrow aims in-/outward and if the angle with the radial direction is less than 20° . Therefore, the fractions of in-/outward flow vectors presented in Fig. 7 do not add up to 100%, since more tangential flows are neglected. At a radial distance of $6 \pm 2 \text{ Mm}$ from the boundary of spot A more than 50% of flow vectors point outward. The average flow speed in this region is about 0.5 km s^{-1} . The region with high-speed outward flows marks the location, where the moat flow around spot A terminates. An exact determination of where the moat flow starts and where it ends strongly depends on the underlying criteria, e.g., photometric or magnetic features, or horizontal proper motions. In Sect. 3.5, we will discuss some properties of moat flow based on the proper motions of MMFs. Sobotka & Roudier (2007) determine that the moat radius is independent of the spot size. However, Balthasar & Muglach (2010) find that the

moat flow terminates at a distance of four times the spot radius – in contrast to three times the spot radius in the present study. Extended statistical studies will help to clarify this issue.

We created two ring-like structures by morphological dilation with a width of 4 Mm, which encircled both spots at a distance of 2 Mm. This ring-like structure starts, where inflows turn to outflows 2 Mm beyond the boundary of spot A, and terminates, where the outflows reach the highest speed. We used these templates to calculate the flows in the immediate neighborhood of spots A and B. These regions were labeled as rings A and B. The velocities for these regions are included in Tab. 1. The flow speed $v_{\text{Ring A}}$ was more than double than that of $v_{\text{Spot A}}$ because of the suppressed convective motions in the spot's interior. The flow speeds in the immediate vicinity of spot B was higher by 30–40% on November 18 and 19. However, on November 22 during the final decay stage of spot B, no major difference between the spot and its closest surroundings were observed.

To effectively visualize the plasma motions we presented high resolution maps of flow speed and azimuth (see Figs. 5 and 6). The speed maps of G-band and Ca II H images are virtually same. The region with G-band bright points exhibits suppressed velocities in both cases. The regions around spot A and the small pore to the west are surrounded by a ring of high velocities (around 0.5 km s^{-1}), where the ordered moat flow terminates. In the azimuth maps of November 18 and 19 outward plasma motions are traceable in these regions. In addition, to gain more insight into inflows and outflows around the spots we computed the divergence of the flow field. The divergence maps are included in the bottom row of Fig. 5. The positive values of divergence refer to outflows, whereas negative values indicate inflows. Negative divergence values are encountered within the boundaries of the sunspots. In contrast small patches of positive divergence encircle the spots. This is indicative of inflows in the sunspots and outflows at their periphery. The area with low divergence values is increasing as the active region is decaying. The presence of a low divergence region could be a signature of the final stages of decay.

3.4. Line-of-sight velocities

The LOS velocities were derived using *Hinode*/SP Fe I spectral data and H α spectra of the VTT Echelle spectrograph. LOS velocities for the Fe I spectral line were calculated using the Fourier phase method (Schmidt et al., 1999). This method makes use of entire line profile and is less sensitive to noise, along with this it takes into account the spectral line asymmetry. To compute the LOS velocity for H α spectra we calculated shifts using parabola fits to the central 50 pixels (0.03 nm), because the H α spectral line is too wide to identify the real continuum. The calculated shifts in both cases were converted to velocities using the Doppler formula. The average photospheric velocity of dark umbral cores was used as the frame of reference. The Fe I $\lambda 656.92 \text{ nm}$ line served as the reference for the H α velocities. The Doppler velocity maps are displayed in the bottom and middle rows of Fig. 8. Redshifts in these maps are positive and blueshifts are negative, hence, areas moving away from the observer are bright, while areas moving toward the observer are dark.

To compute velocities for various solar features we used an intensity mask generated using G-band images. The values are compiled in Tab. 1. On November 18 and 20 in the Fe I Doppler velocity maps strong photospheric downflows were observed at edges of spot B. The average downflow velocity in these regions is about 2.5 km s^{-1} . In all maps a gray patch of near zero veloc-

ity was observed in the central FOV, which became more prominent on the last two days of observation. We identify this region with abnormal granulation (see e.g., de Boer & Kneer, 1992), in which convection is still strongly inhibited by the presence of (dispersed) magnetic fields.

In case of H α LOS velocities no conspicuous features were visible in the velocity maps, except on November 18 when we observed a radial filamentary structure around spot A in H α line core intensity maps, which resembled a superpenumbra. At the footpoints of the dark H α filaments, we measure downflows from about 3.5 up to 4.5 km s^{-1} , which we interpret as an inverse Evershed flow (Maltby, 1975). Tightly wound superpenumbral spirals are only predicted for spots with radii larger than 8 Mm, whereas spot A was compact with a radius of 4 Mm. The downward chromospheric velocities at the edge of spot A are compatible with the MHD model of superpenumbral flows presented by Peter (1996).

3.5. Magnetic fields

In addition to the photometric evolution shown in Fig. 3, we also computed the flux contained in the active region as shown in Fig. 4. Since only HMI LOS magnetograms were available (processing of the vector magnetograms is still under way). We took the measured magnetic field strength at face value and only carried out a geometrical correction to yield the proper average values of the magnetic flux. The geometrical correction only applies to the surface area covered by a pixel, which can simply be achieved by dividing the magnetic field strength by $\mu = \cos\theta$. Signatures of geometric projection effects can be seen when the active region was close to the east limb, and the angle between LOS and shallow penumbral field lines leads to an apparent polarity reversal. Consequently, the positive and negative flux gradients have opposite signs, while the total flux remained almost constant for the first 30 hours until projection effects become less severe. To compute the temporal evolution of magnetic flux, we created a binary template, which only contained pixels above/below ± 50 Gauss in the HMI magnetograms. Morphological erosion with a 1-Mm kernel was applied to the template three times to eliminate small, isolated flux concentrations. Finally, we used morphological dilation with a 5-Mm kernel to include the strong magnetic fields in the immediate neighborhood of active region NOAA 11126. In this way, we avoided a bias, which could be introduced by weak magnetic fields, which do not belong to the active region but are contained within the FOV shown in Fig. 2.

The growth rates of the magnetic flux are 2.66 , 1.98 , and $1.09 \times 10^{13} \text{ Wb day}^{-1}$ for the total, positive, and negative flux, respectively. The negative flux showed a monotonous rise until about 06:00 UT on November 16, whereas the positive flux increased with a twice steeper slope, stopped a day earlier, and turned to a shallower slope until the end of November 17. On average the positive flux was three times larger than the negative one. However, using adaptive thresholding and morphological image processing tools, we only measured the flux in the immediate vicinity of the sunspots. The missing negative flux required for flux balance has to be contained in flux concentration beyond the immediate neighborhood of the sunspots. The decay rates of the magnetic flux are four to five times lower than the growth rates and amount to 0.66 , 0.47 , and $0.23 \times 10^{13} \text{ Wb day}^{-1}$ for the total, positive, and negative flux, respectively. A linear fit to the data was used and despite some deviations from a linear trend, there is no indication for a parabolic (or any other) decay law. The decay rates of the present study are in agreement with Kubo

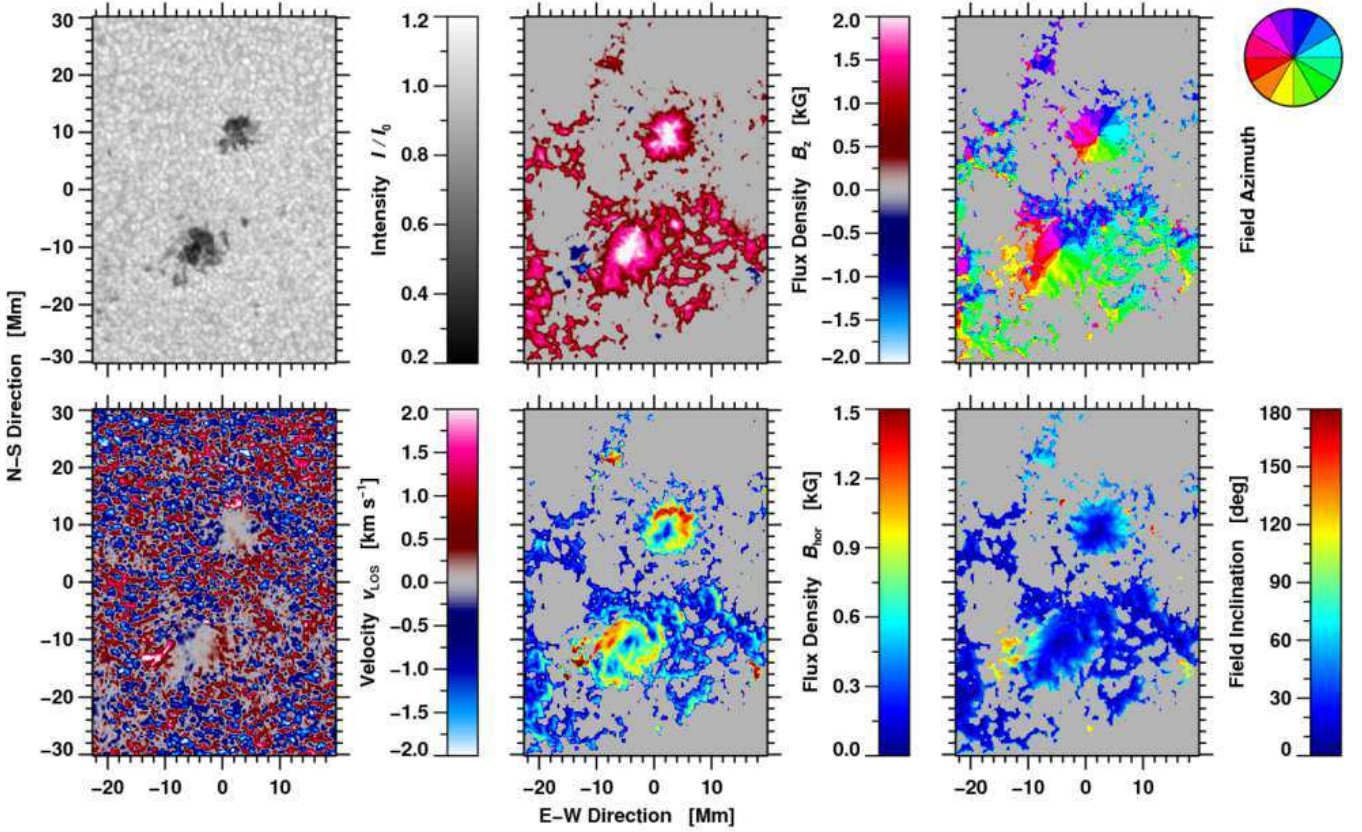


Fig. 9. Maps of physical parameters derived using SIR-code for *Hinode*/SP scan on 2010 November 18 (from top-left to bottom-right) normalized intensity I/I_0 , vertical component of magnetic flux density B_z , magnetic field azimuth ϕ , Doppler velocity v_{LOS} , horizontal component of magnetic flux density B_{hor} , and magnetic field inclination γ .

et al. (2008) who report rates on the order of 10^{13} Wb day $^{-1}$ and discusses the magnetic flux loss rate in a decaying active region.

The SIR-code (Stokes Inversion based on Response functions) developed by Ruiz Cobo & del Toro Iniesta (1992) was used to invert the *Hinode*/SP spectra. We restrict ourselves to the more sensitive line Fe I $\lambda 630.25$ nm ($g_{\text{eff}} = 2.5$). The starting model covers the optical depth range $+1.0 \leq \log \tau \leq -4.4$. A limb-darkening factor is considered according to Eq. 10 of Pierce & Slaughter (1977). We assume a constant macroturbulence of 1 km s^{-1} and a fixed straylight contribution of one percent. The inversions deliver the temperature stratification with four nodes $T(\tau)$, the total magnetic flux density B_{tot} , the magnetic inclination γ and azimuth ϕ , and the Doppler velocity v_{LOS} constant with height (one node for each of these physical parameters).

The magnetic azimuth ambiguity must be solved after the inversions. For the first two days when we observed two major pores/small sunspots, we assumed two azimuth centers (see Balthasar, 2006). For the other days it is sufficient to assume one azimuth center away from the pores in the direction towards disk center. The magnetic field in such small pores is more or less vertical to the solar surface so that on these days the field is sufficiently inclined with respect to the LOS that such an assumption is justified. If the expected azimuth ϕ deviates by more than 90° and less than 270° from the calculated one, we correct it by 180° . Finally, we rotate the magnetic vector with respect to the local solar frame. For a few locations, it happens that there is a sudden change of sign in the Cartesian components of the magnetic vector. This problem is solved by an additional correction of the LOS-azimuth. To be on the safe side, we additionally

apply to data of November 18 the code provided by Leka et al. (2009), which minimizes $|J_z| + |\nabla B|$ to solve the azimuth ambiguity. Pixels, where the integrated circular and the integrated linear polarization are below 0.006, are excluded from the further analysis of the magnetic field. We finally use the magnetic vector field in the local solar frame. The results of the SIR-inversion for November 18 are depicted in Fig. 9.

The vertical magnetic flux density B_z in the ROI is predominantly positive and points outwards. The only significant patches of negative polarity were found on November 18 on the eastern side of spot B. Penumbra filaments connect spot B to several magnetic knots of negative polarity. In addition, we measure Evershed flows with velocities $v_{\text{LOS}} > 2 \text{ km s}^{-1}$. On smaller spatial scales, we find MMFs in the vicinity of spot A. They are mostly of type II (unipolar with the same polarity as the spot) but a few scattered U-shaped type I MMFs (bipolar with the inner footpoint of opposite polarity of the spot) were observed as well. No type I MMFs were observed near spot B.

Since the time cadence of *Hinode*/SP scans is about 12 min, we used SDO/HMI magnetograms with a cadence of 45 s to study the dynamics of MMFs. Space-time slices are an option to visualize local changes of the magnetic flux in a time-series. The continuous coverage of HMI magnetograms allowed us to depict in Fig. 10 the temporal evolution of the magnetic flux around spot A during a 12-hour period on 2010 November 18. The magnetic flux changes were recorded within two 0.5-Mm wide annuli of 5.75 Mm (bottom panel) and 7.25 nm (top panel) radius, respectively. Note that the linear scale of the the ordinate in Fig. 10 is 38 Mm and 47 Mm for the inner and outer ring, respectively. The inner ring corresponds to the location, where

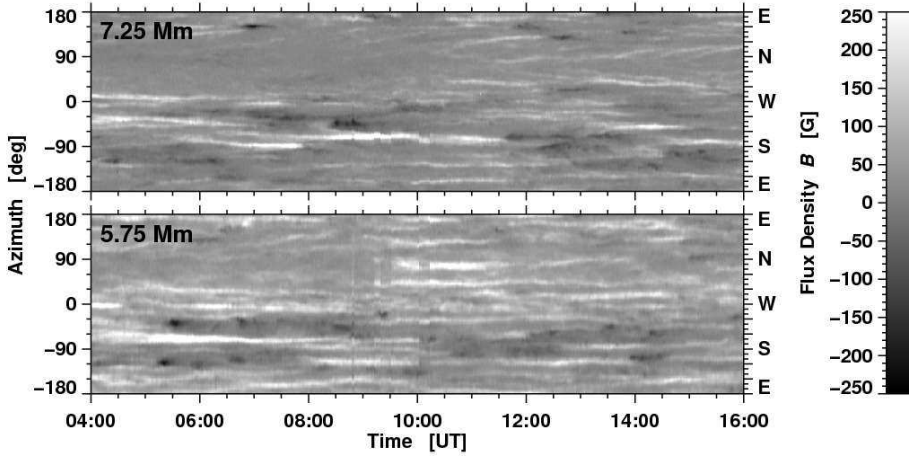


Fig. 10. Space-time slices showing the temporal evolution of the magnetic flux along annuli with radii of 5.75 Mm (*bottom*) and 7.25 Mm (*top*), respectively, which are centered on spot A. HMI magnetograms with a cadence of 45 s covered a period of 12 hours starting at 04:00 UT on 2010 November 18. The annulus with a widths of 0.5 Mm was cut open in the East and then transformed to straight line so that the southern part of the spot is mapped to the lower half of the space-time map. The heliographic direction is indicated on the axis to the right.

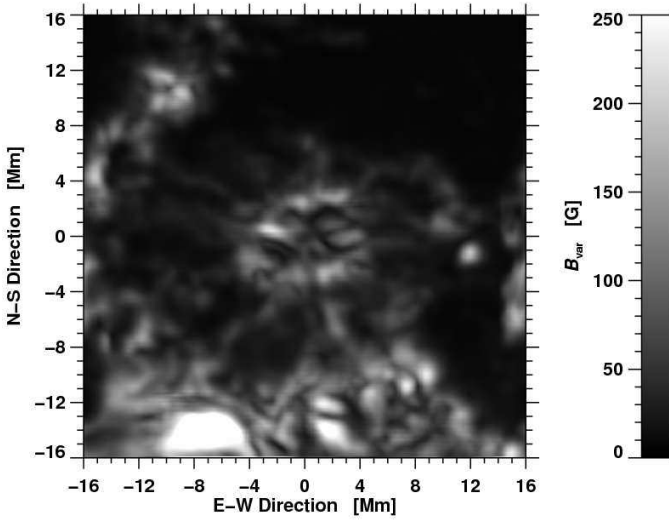


Fig. 11. Local, background-subtracted variation of the magnetic flux B_{var} around spot A on 2010 November 18.

the strongest outflows were observed (see Fig. 7). The outer ring marks the site, where the largest fraction (about 8%) of the annulus is covered by negative-polarity features.

Within a radial distance from 4–10 Mm from the center of spot A, only about 5% of the magnetic flux observed during 12-hour period is of negative polarity. Negative-polarity MMFs are weaker by about 20% as compared to MMFs of opposite polarity. Negative flux elements are most prominent in the southern half of spot A and absent in the northern half. The most notable difference between positive- and negative-polarity features is the morphology. Negative-polarity features can be tracked in space-time slices for only about 15–30 min, i.e., they are strongly localized. Time-lapse movies show that these negative-polarity features are mostly type I MMFs. The positive polarity appears first in the space-time slices (to the left) followed by the negative polarity. The appearance of the positive-polarity features is very different. Horizontal striation can be seen for several hours. They can abruptly (dis-)appear and in a few cases merging as well as splitting of the striae can be observed. In time-lapse movies, type II MMFs are moving away from spot A along radial paths on top of a background of positive flux.

The temporal variation of the magnetic flux above/below the local background is given by $B_{\text{var}} = \langle |B - \langle B \rangle| \rangle$, where $\langle \dots \rangle$ indicates a temporal average. To compute the temporal average in

Fig. 11, we used the same 12-hour time-series of HMI magnetograms that was used to create Fig. 10. The strongest changes occur at the periphery of spot A, where also the horizontal magnetic field B_{hor} is strongest as can be seen in Fig. 9. This correspondence also applies to the feature of strong horizontal field to the north-east of spot A, which belongs to the (chromospheric) network. The most notable features in Fig. 11 are, however, several spoke-like structures with a length of about 10 Mm, which extend from spot A all the way out to the border of the supergranule surrounding the spot. These elongated structures are the signatures of MMFs streaming from the spot along identical paths (Harvey & Harvey, 1973) towards the supergranular boundary. However, the distance traveled is much shorter as Harvey & Harvey (1973) observed for mature sunspots. Therefore, we conclude that the preferred paths of MMFs are a phenomenon, which can be observed even in the final stages of sunspot decay. The traces left by MMFs in the variance of the magnetic field around its background B_{var} are most prominent on the eastern side of the spot. They also match the wagon-wheel structure discussed in the context of the time-averaged Ca II H images in Sect. 3.2. Finally, the preference of MMFs for distinct radial channels connecting the sunspots' magnetic fields to the strong network fields was also noticed by Hagenaar & Shine (2005).

Maps similar to Fig. 9 were computed for each day so that we could study the evolution of the magnetic field. The strongest horizontal magnetic flux densities B_{hor} are observed in the immediate surroundings of spots A and B as long as the spots are compact (November 18 and 19). They symmetrically enclose the entire boundary of the spots. Once spot A had disappeared and spot B started to fragment, this symmetry is broken most evidently on November 20, when strong horizontal fields were present at the western side of spot B. This corresponds to a time when a rudimentary penumbra was present. Whenever indications of penumbral filaments were observed during the decay of the sunspots, inclined magnetic field lines and Evershed flows were present at the same time (cf., Leka & Skumanich, 1998; Yang et al., 2003).

The magnetic field lines spread out symmetrically from the center of the spots on November 18 and 19. Such well defined azimuth centers can still be found in the later decay stages of spot B. Even though these region are no longer circular and become elongated. Smaller azimuth centers are also observed to the east of spot B on November 19. These centers are associated to several magnetic knots.

The Doppler velocity v_{LOS} is suppressed in the presence of strong magnetic features. Starting on November 20, the veloc-

ity pattern associated with the magnetic fields changes. Positive Doppler velocities occupy more and more of the magnetic region. This coherent pattern was also observed in the divergence maps (bottom row of Fig. 5) and the horizontal flow maps (Figs. 5 and 6). Indeed, considering that the region is approaching the limb, some of the Doppler velocities can be interpreted as a coherent proper motion of the magnetic region towards the south-west (cf. the azimuth maps of the horizontal proper motions). In summary, during the final stages of sunspot decay, the three-dimensional flow field, in regions previously occupied by strong magnetic fields, significantly differs from granular flow patterns or regions of reduced velocities in the presence of G-band bright points. Since we are only presenting a case study, the question remains, if this intriguing flow pattern is a typical feature of sunspot decay.

4. Conclusions

We have presented a detailed account of the final stages in the decay of the active region NOAA 11126, which did not obey the Hale-Nicholson polarity law (e.g., Zirin, 1988). Since only one out of ten active regions shows such a behavior (Howard, 1990) and we only present a case study, our results might not be representative for sunspot decay in general. However, space missions such as *Hinode* and SDO provide nowadays data of sufficient coverage, resolution, and cadence that statistical properties of sunspot decay become accessible. Furthermore, previous studies of non-Hale regions (e.g., López Fuentes et al., 2000, and reference therein) were centered on flux emergence, δ -spots, and strong solar flares. The present study can consequently be considered as an extension of these studies with a focus on a much quieter magnetic field topology, which might be representative for the lower solar activity during cycle No. 24 (Petrovay, 2010; Nielsen & Kjeldsen, 2011).

The major findings of our study can be summarized as follows: (1) MMFs were observed in the vicinity of spot A until it decayed. Mostly type II and a few interspersed U-shaped type I MMFs contributed to the observed moat flow, which also left a clear signature in the time-averaged Ca II H images (Martínez Pillet, 2002). (2) Even though penumbral filaments had almost completely disappeared in photospheric G-band images of spot A on November 18, H α line core images clearly exhibited a structure reminiscent of a superpenumbra. Thus, filamentary structures including the inverse Evershed flow (Maltby, 1975; Georgakilas & Christopoulou, 2003) might be more persistent in the chromosphere. (3) We have also observed MMFs in the vicinity of a tiny pore with a diameter of about 2 Mm, which did not show any indication of penumbral filaments. Such an observation argues strongly against a close tie between Evershed flows and MMFs (cf., Vargas Domínguez et al., 2008, 2010; Cabrera Solana et al., 2006). Rempel (2011) argues based on MHD simulations of sunspots that penumbral flows can be separated in two components, where the shallow one corresponds to the Evershed flow and the deeper one is related to moat flow. (4) The strong rotation and twist seen in spot B might explain, why this trailing spot never advected sufficient magnetic flux to establish more than a rudimentary penumbra and remained highly fragmented during its entire life cycle. (5) The photospheric and chromospheric maps of horizontal flows show a peculiar pattern, once the last dark feature of the active region has disappeared. In general, the flow field in this region is less structured than regions covered by granulation, i.e., the dispersed magnetic field still significantly affects the convective pattern. Chromospheric flows have increased notably compared to times when spots and

pores were still present. Most prominently, a contiguous area of low divergence appears towards the end of sunspot decay.

Acknowledgements. *Hinode* is a Japanese mission developed and launched by ISAS/JAXA, collaborating with NAOJ as a domestic partner, NASA and STFC (UK) as international partners. Scientific operation of the *Hinode* mission is conducted by the *Hinode* science team organized at ISAS/JAXA. This team mainly consists of scientists from institutes in the partner countries. Support for the post-launch operation is provided by JAXA and NAOJ (Japan), STFC (UK), NASA, ESA, and NSC (Norway). The SDO/HMI images are provided by the Joint Science Operations Center (JSOC) Science Data Processing (SDP). The Vacuum Tower Telescope at the Spanish Observatorio del Teide of the Instituto de Astrofísica de Canarias is operated by the German consortium of the Kiepenheuer-Institut für Sonnenphysik in Freiburg, the Leibniz-Institut für Astrophysik Potsdam, and the Max-Planck-Institut für Sonnensystemforschung in Katlenburg-Lindau. MV expresses her gratitude for the generous financial support by the German Academic Exchange Service (DAAD) in the form of a PhD scholarship. CD was supported by grant DE 787/3-1 of the German Science Foundation (DFG). CL and HW were supported by NSF grants AGS 08-19662 and AGS 08-49453, and NASA grants NNX 08AQ90G and NNX 08AJ23G. ND was supported by NASA grant NNX 08AQ32G. The authors would like to thank Drs. Alexandra Tritschler and Klaus G. Puschmann as well as the referee Dr. Luis Bellot Rubio for carefully reading the manuscript and providing ideas, which significantly enhanced the paper.

References

- Balthasar, H. 2006, A&A, 449, 1169
- Balthasar, H. & Muglach, K. 2010, A&A, 511, A67
- Bellot Rubio, L. R., Tritschler, A., & Martínez Pillet, V. 2008, ApJ, 676, 698
- Bentley, R. D. & Freeland, S. L. 1998, in ESA Special Publication, Vol. 417, Crossroads for European Solar and Heliospheric Physics. Recent Achievements and Future Mission Possibilities, 225–228
- Bumba, V. 1963, Bull. Astron. Inst. Czech., 14, 91
- Cabrera Solana, D., Bellot Rubio, L. R., Beck, C., & del Toro Iniesta, J. C. 2006, ApJL, 649, L41
- Couvidat, S., Schou, J., Shine, R. A., et al. 2011, Sol. Phys., 33
- de Boer, C. R. & Kneer, F. 1992, A&A, 264, L24
- Deng, N., Choudhary, D. P., Tritschler, A., et al. 2007, ApJ, 671, 1013
- Deng, N., Xu, Y., Yang, G., et al. 2006, ApJ, 644, 1278
- Denker, C., Deng, N., Tritschler, A., & Yurchyshyn, V. 2007, Sol. Phys., 245, 219
- Denker, C., Johannesson, A., Marquette, W., et al. 1999, Sol. Phys., 184, 87
- Freeland, S. L. & Handy, B. N. 1998, Sol. Phys., 182, 497
- Georgakilas, A. A. & Christopoulou, E. B. 2003, ApJ, 584, 509
- Hagenaar, H. J. & Shine, R. A. 2005, ApJ, 635, 659
- Harvey, K. & Harvey, J. 1973, Sol. Phys., 28, 61
- Howard, R. F. 1990, Sol. Phys., 126, 299
- Ichimoto, K., Lites, B., Elmore, D., et al. 2008, Sol. Phys., 249, 233
- Kosugi, T., Matsuzaki, K., Sakao, T., et al. 2007, Sol. Phys., 243, 3
- Kubo, M., Lites, B. W., Shimizu, T., & Ichimoto, K. 2008, ApJ, 686, 1447
- Leka, K. D., Barnes, G., Crouch, A. D., et al. 2009, Sol. Phys., 260, 83
- Leka, K. D. & Skumanich, A. 1998, ApJ, 507, 454
- López Fuentes, M., Demoulin, P., Mandrini, C. H., & van Driel-Gesztelyi, L. 2000, ApJ, 544, 540
- Maltby, P. 1975, Sol. Phys., 43, 91
- Martínez Pillet, V. 2002, AN, 323, 342
- Meyer, F., Schmidt, H. U., Wilson, P. R., & Weiss, N. O. 1974, MNRAS, 169, 35
- Nielsen, M. L. & Kjeldsen, H. 2011, Sol. Phys., 270, 385
- Peter, H. 1996, MNRAS, 278, 821
- Petrovay, K. 2010, Living Rev. Sol. Phys., 7, 6
- Petrovay, K. & van Driel-Gesztelyi, L. 1997, Sol. Phys., 176, 249
- Pierce, A. K. & Slaughter, C. D. 1977, Sol. Phys., 51, 25
- Rempel, M. 2011, ApJ, 729, 5
- Roupe van der Voort, L., Bellot Rubio, L. R., & Ortiz, A. 2010, ApJ, 718, L78
- Rucklidge, A. M., Schmidt, H. U., & Weiss, N. O. 1995, MNRAS, 273, 491
- Ruiz Cobo, B. & del Toro Iniesta, J. C. 1992, ApJ, 398, 375
- Rutten, R. J., de Wijn, A. G., & Sütterlin, P. 2004, A&A, 416, 333
- Schlichenmaier, R., Rezaei, R., Bello González, N., & Waldmann, T. A. 2010, A&A, 512, L1
- Schmidt, W., Stix, M., & Wöhl, H. 1999, A&A, 346, 633
- Schou, J., Borrero, J. M., Norton, A. A., et al. 2010, Sol. Phys., 177
- Shine, R. A., Title, A., Frank, Z., & Scharmer, G. 1996, Bull. Am. Astron. Soc., 28, 871
- Sobotka, M., Bonet, J. A., & Vázquez, M. 1993, ApJ, 415, 832
- Sobotka, M. & Roudier, T. 2007, A&A, 472, 277

- Strous, L. H., Scharmer, G., Tarbell, T. D., Title, A. M., & Zwaan, C. 1996, A&A, 306, 947
- Tsuneta, S., Ichimoto, K., Katsukawa, Y., et al. 2008, Sol. Phys., 249, 167
- Vargas Domínguez, S., de Vicente, A., Bonet, J. A., & Martínez Pillet, V. 2010, A&A, 516, A91
- Vargas Domínguez, S., Rouppe van der Voort, L., Bonet, J. A., et al. 2008, ApJ, 679, 900
- Verma, M. & Denker, C. 2011, A&A, 529, A153
- Wachter, R., Schou, J., Rabello-Soares, M. C., et al. 2011, Sol. Phys., 19
- Yang, G., Xu, Y., Wang, H., & Denker, C. 2003, ApJ, 597, 1190
- Zirin, H. 1988, Astrophysics of the Sun
- Zuccarello, F., Romano, P., Guglielmino, S. L., et al. 2009, A&A, 500, L5